Proceedings of the 28th IEEE
EMBS Annual International Conference
New York City, USA, Aug 30-Sept 3, 2006

Magnetic Microactuators for MEMS-Enabled Ventricular Catheters for Hydrocephalus

Selene A. Lee, M.S.[1, 2], Daniel J. Vasquez, M.S. [4], Marvin Bergsneider, M.D.[1, 2, 3], Jack W. Judy, Ph. D.[1, 2, 4]
[1] NeuroEngineering Training Program, [2] Biomedical Engineering Interdepartmental Program,
[3]Neurosurgery, School of Medicine, [4] Electrical Engineering Department,
University of California, Los Angeles
Los Angeles, CA 90095 USA

***Abstract*- The most common treatment for patients with hydrocephalus is the surgical implantation of a cerebrospinal-fluid (CSF) shunt. Unfortunately, this device, which is critical for lowering intracranial pressure, has a substantial failure rate (40% in the first year). A leading cause of failure is the obstruction of the ventricular catheter. The goal of this project is to design a ventricular catheter that will resist occlusion through the use of micromachining and micro-electro-mechanical systems (MEMS) technologies. We designed, fabricated, and tested magnetic microactuators. The theoretical results show that the fabricated microactuators can produce the force necessary to remove an adherent cellular layer grown over the actuator surface. By integrating the microactuators into the catheters, we hope to produce an improved catheter with the ability to actively combat the health-threatening occlusion process.**

I. Introduction and Motivation

One in every 500 newborns is afflicted by hydrocephalus, a condition characterized by an abnormal accumulation of cerebrospinal fluid (CSF) due to an imbalance between CSF production and absorption [1]. In addition, hydrocephalus may also be acquired later in life due to incidents such as head trauma or tumor development. Fortunately, treatments have greatly increased the probability for hydrocephalic patients to achieve normal intelligence and to lead a normal life. Specifically, one of the most common treatments for patients with hydrocephalus is the surgical implantation of a CSF shunt [2], which consists of a ventricular catheter, valve, and distal catheter that drains excess CSF from the ventricles to the abdomen (Fig. 1) [3].

Patients who receive implanted shunts are dependent on the device functioning properly. Unfortunately, this device, which is so critical for managing hydrocephalus, has a substantial failure rate and a malfunctioning shunt can be a life-threatening condition [2]. Shunt-replacement surgeries can cause temporary and sometimes significant morbidity. Each successive shunt revision may cause brain injury and increases the risk of shunt infection. On average, 85% of people with shunts have at least two shunt-revision surgeries.

A leading cause of shunt failure is obstruction of the ventricular catheter. Ventricular catheter obstruction is caused primarily by ventricular collapse due to overdrainage, choroid-plexus tissue migration and ingrowth, and gradual cellular accumulation in flow holes. To address the problem of overdrainage, pressure-regulating valves have been integrated into the device, while tissue ingrowth can be avoided with better catheter placement. This work is focused primarily on proximal ventricular-catheter obstruction caused by gradual cellular accumulation in the flow holes.

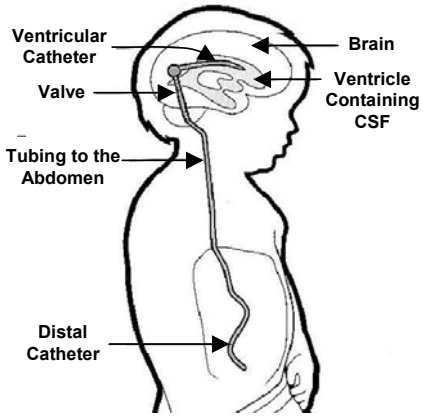

Figure 1. Overall shunt composition and placement.

Pathological studies have shown that the cellular composition of catheter obstructions consists mainly of calcium formation, red blood cells, ependymal cells, and inflammatory tissue [4-12]. The most probable sources of cell accumulation leading to catheter obstruction are inflammatory cells. Several researchers suggested that varying rates of catheter occlusion due to cell accumulation may result from a variation in the delayed hypersensitivity response [7;11;13].

Based on the hypothesis that protein and inflammatory-cell interaction is the primary etiology of ventricular-catheter occlusion, we acknowledge that cellular adhesion is an ongoing yet slowing accumulating process. We propose to integrate magnetic microactuators that are capable of mechanically maintaining a clear ventricular catheter without requiring an implanted power supply into the shunt. Our device uses a miniaturized actuator to physically sweep cells from the surface, continually renewing the catheter surface and producing a patent catheter after each actuation. By accomplishing this goal, we hope to realize a next-generation hydrocephalus shunt that will prevent or significantly delay shunt obstruction and thus reduce the frequency of shunt-replacement surgeries.

II. Magnetic Microactuators

A. Design

We previously demonstrated magnetic microactuators appropriate for use in biological fluids [4-15]. Building upon our investigation of ventricular-catheter obstruction and our experience with magnetic MEMS, we seek to realize a self-clearing ventricular catheter through the integration of magnetic microactuators. Micromachining techniques can be used to incorporate magnetic microactuators onto substrates that, in turn, can be integrated with existing catheters to produce MEMS-enabled catheters that actively resist occlusion formation. The ability to use a remote magnetic field to control the movement of the implanted magnetic microactuators eliminates concerns about electrical-lead failure and the incorporation and maintenance of an implanted power supply. In addition to functioning in a fluidic environment, the magnetic microactuators must be capable of actuating through a layer of aggressive cellular growth. For this reason, we must adapt the previously developed magnetic microactuators for use in a dense cellular environment. After we design and fabricate the magnetic microactuators, we will verify their ability to actuate within a layer of cultured adherent cells.

Prototype magnetic microactuators are designed and fabricated to test actuation in a cellular environment. A nickel magnet actuates a layer of silicon nitride that is anchored to the substrate by two silicon nitride torsion beams (Fig. 2).

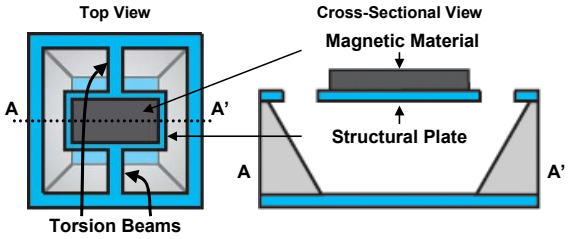

Figure 2. Top and cross-sectional view of microactuator design.

The scale of the MEMS prototype is designed for direct integration into the 1-mm-diameter pore holes of commercial catheters. To investigate the impact of dimensions of the magnetic microactuator, we designed an array of microactuators with varying magnetic-plate sizes and torsion-beam widths. Each microactuator array contains a total of 25 microactuators, one for each combination of plate widths (600, 650, 700, 750, and 800 μm), plate lengths (200, 300, 400, 500, and 600 μm), and torsion-beam widths (20, 40, 60, 80, and 100 μm). The final layout contains ten copies of each actuator on a single 100-mm-diameter substrate.

C. Fabrication

The actuators are fabricated on a 100-mm-diameter single-crystal <100> silicon wafer. After cleaning and etching away any native oxide layer with hydrofluoric acid (HF), we deposit a 1-μm-thick layer of low-stress nitride on both sides of the wafer by low-pressure chemical-vapor deposition (LPCVD) (Figure 3, Step 1). In the first photolithography step, the nitride is patterned with thin AZ5214 photoresist to define the boundaries for the structural layer of the actuator. The nitride is then selectively etched using an STS Multiplex Advanced Oxide Etcher (AOE) (Figure 3, Step 2). A second dry etch is performed in a Deep Reactive Ion Etcher (DRIE) to create 10-μm-deep trenches in the silicon wafer, defining the mechanical structure and facilitating device release in the final steps of fabrication (Figure 3, Step 3). The protective photoresist is then removed with a plasma etch in a downstream Tegal Asher.

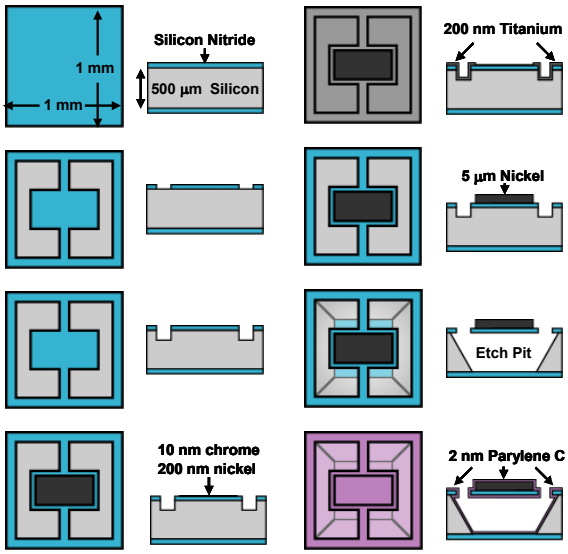

Figure 3. Fabrication process for the magnetic microactuators.

Next, we perform the second photolithography step by depositing a thick photoresist (SPR 220-7.0, spun at 3000 RPM) in a second pattern that exposes the areas of the wafer for the metal adhesion (10 nm of chrome, followed by 100 nm of nickel). We use the thicker photoresist (SPR 220-7.0, spun at 3000 RPM) to completely cover the surface of the 10-μm-deep trenches. After the metal is deposited using a CHA e-beam metal evaporator, the photoresist as well as the metal deposited on the photoresist are removed through a lift-off process (Figure 3, Step 4). A 200-nm-thick titanium conduction layer is evaporated over the front side of the entire wafer to connect the chrome and nickel seed layers (Figure 3, Step 5).

Using the same mask we used to deposit the chrome and nickel, we pattern the titanium with a thick photoresist (SPR-7.0) to define a 10-μm-thick plating mold for the nickel magnet. Before electrochemically plating the nickel layer, a quick 90-second dip in a diluted (200:1) HF solution removes the titanium at the base of the photoresist mold to expose the nickel seed layer in preparation for plating. We then place the wafer in a nickel-plating solution (1-M nickel sulfamate and 0.4-M boric acid) and pass a constant current density of 10 mA/cm^2 to the seed layer for 25 minutes.

After plating a 5-µm-thick nickel magnet, the photoresist mold is removed by rinsing the wafer successively in acetone, methanol, iso-propanol, and finally de-ionized water. The titanium conduction layer is completely removed by dipping for 4 minutes in the diluted HF solution (Figure 3, Step 6).

A 12-hour potassium hydroxide wet etch (heated to 72 °C) releases the actuators and defines the pits for cell growth in one step (Figure 3, Step 7). To improve biocompatibility, the actuators are fully coated in a conformal 200-nm-thick layer of parylene C polymer (Figure 3, Step 8). The completed devices are shown in Figure 4.

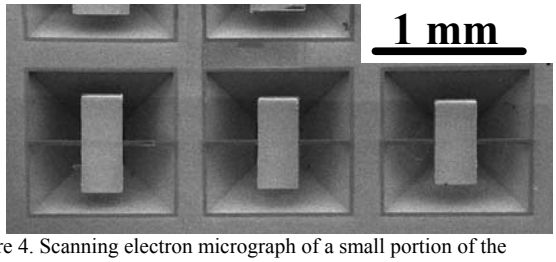

Figure 4. Scanning electron micrograph of a small portion of the microactuator array with various magnet sizes and torsion beams.

D. Device Characterization

We characterized the magnetic properties of the electrochemically-plated nickel magnet using a vibrating-sample magnetometer (Digital Measurement Systems, Westwood, MA, USA). A complete *B-H* loop was obtained and the magnetization of our magnetic elements at the magnetic field used for our characterization (~6 kA/m) was 0.37 T. Next, we measured the angle of rotation produced by each microactuator as a function of an applied magnetic field. The laser-deflection-based experimental setup used to obtain these measurements is illustrated in Fig. 5 and the measurements are given in Fig. 6. The theory governing these magnetic microactuators is well developed [14-15]. We calculated the deflection using Eq. 1, which is given by

$$\frac{\left(\hat{M}\times\hat{H}\right)\cdot V_{mag}}{k_{\phi}} = \phi \quad , \qquad (1)$$

with magnetization $\hat{M}$, applied field $\hat{H}$, magnet volume V_{mag}, angular torsion-beam stiffness k_{ϕ}, and angular deflection ϕ.

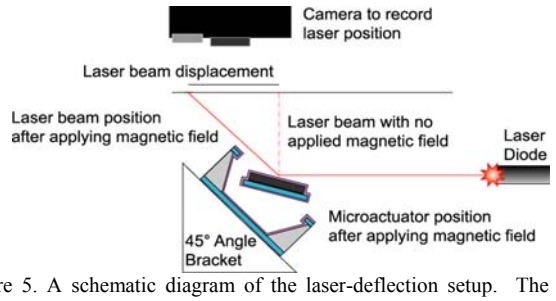

Figure 5. A schematic diagram of the laser-deflection setup. The laser-beam deflection is recorded for the microactuator given an applied magnetic field.

E. Cellular Removal

Typical values for shear stresses required to remove a layer of adherent cells using jet impingement fall in the range of 300 to 350 µN/mm^2, while other adhesion tests produce values lower than 350 µN/mm^2 [16, 17].

We measured the magnetic torque produced by our devices, then used finite-element-method (FEM) analysis to determine the tensile forces experienced by a cellular layer attached between the actuator and the surrounding substrate. By describing the adherent-cell layer attached to the magnetic microactuator as a network of interconnected springs and solving for the tensile forces experienced at different locations on the network, we were able simulate the removal process.

III. Results and Discussion

A. Device Characterization

Due to the layout design and the microfabrication process, only microactuators with 20-µm-wide and 40-µm-wide torsion beams were fully released by the KOH wet etch. As a result, the microactuators with torsion-beam widths ranging from 60 to 100 were not characterized. The performance of the successfully released microactuators was measured (Fig. 6) using the optical-characterization methods described in Fig. 5. Using the values measured for the magnetization, magnetic field, and magnetic volume, we predicted an angular deflection using Eq. 1. Similarly, given that the magnetic torque can be expressed as

$$\tau_{\mathrm{magnetic}} = \left(\hat{M}\times\hat{H}\right)\cdot V_{\mathrm{mag}} \quad , \qquad (2)$$

we determined the magnetic torque produced by each device.

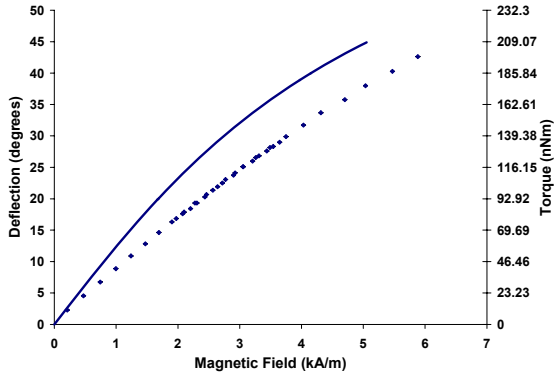

Figure 6. Theoretical and measured (n = 3) deflection and torque for applied external magnetic field of a microactuator with a magnet volume of 200 × 650 × 5 µm^3, 20-µm-wide torsion beams, and 0.37 T saturation magnetization. Since the average standard deviation for the deflection measurements is 8.1 × 10^{-8} degrees, the error bars are hidden by the data symbols. We calculated theoretical deflection using a constant value for material magnetization, which may explain the discrepancies between the theoretical and measured values.

B. Cellular Removal

A typical spring constant for a cell was determined from previous studies to be on the order of 0.25 N/m [18].

Given the force adhesion limit of 350 μN/mm^2 and a typical cell adhesion area of 78.54 μm^2 (diameter of 10 μm), one can calculate a maximum cell deformation of 0.15 μm before adhesion is lost. For a torsional microactuator with a 200×650-μm^2 plate inside a 1×1-mm^2 hole, 17.5 cell lengths exist between the edge of the actuator and the substrate. The cell layer can accommodate a total deformation of 2.625 μm. To produce this deformation, a plate must deflect 4.18º.

The simulation (Fig. 7) shows that the highest tensile forces are found at the corners of the actuating plate. Using the cellular adhesion values from the literature, we calculated the magnetic torque required to overcome typical cellular-adhesion forces. For the microactuator geometry given above, the actuation torque must exceed approximately 0.63 nNm. Given a 5-μm-thick magnet made of a ferromagnetic material with a saturation magnetization of 0.37 T, the required magnetic field is 0.59 kA/m.

As mentioned above, each simulation assumes a single layer of cells. Should a thicker layer of adherent cells, tissue, and/or debris accumulate, it is likely the values for the required torque and magnetic field would also increase. However, given that the microactuators fabricated as part of this work are capable of generating 1,000 times more torque, it is fully expected that the microactuator will be capable of breaching such occlusions.

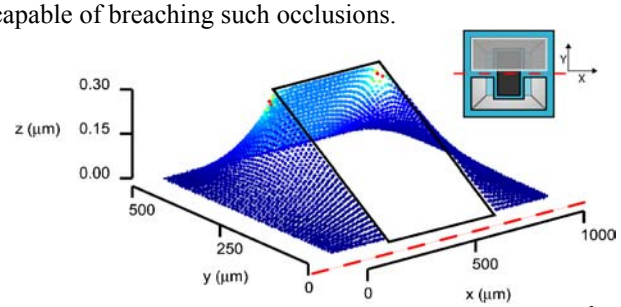

Figure 7. Simulation of an actuator with a magnet (200 × 650 × 5 μm^3) and 20-μm-wide torsion beams rotating through a layer of cells. The shaded region of the top view diagram in the upper-right corner indicates the portion of the actuator shown in the simulation. The dotted line shows the location of the torsion axis. Note that the *z*-axis scale is different from the *x* and *y* axes.

IV. Conclusion

We successfully designed, fabricated, and characterized magnetic microactuators as the first step towards developing a MEMS-enabled ventricular catheter for hydrocephalus. Our model and experimental results lead us to believe that our devices can produce the forces required overcome the typical cell-adhesion values found in the literature. At this time, attempts to grow adherent cells over the actuator surface have been unsuccessful, however we will continue to investigate methods for cellular-layer formation.

By producing a self-clearing MEMS catheter, we will greatly decrease the probability of shunt obstruction. In turn, it is hoped patients will require fewer replacement surgeries, face less risk and stress associated with surgeries, and spend more time enjoying the benefits of a properly functioning shunt.

Acknowledgements

This work was supported by the UC Discovery Program, under award number #BIO-ELE04-10433, the NIH National Research Service Award Fellowship (#NS052044-01), and the Neuroengineering Training Program an NSF IGERT (#9972802).

References

[1] National Institute of Neurological Disorders and Stroke. NINDS Hydrocephalus Information Page. http://www.ninds.nih.gov/health_and_medical/disorders/hydrocephalus.htm.

[2] J.M. Drake, *The Shunt Book* Cambridge: Blackwell Science, 1995.

[3] Spinal Bifidia and Hydrocephalus Association of Nova Scotia. Hydrocephalus Information Page. http://www.chebucto.ns.ca/health/ sbans/hydrocephalus.html.

[4] H.L. Brydon, R. Bayston, R. Hayward, and W. Harkness, "The effect of protein and blood cells on the flow-pressure characteristics of shunts," *Neurosurgery*, vol. 38, no. 3, pp. 498-504, 1996.

[5] M.R. Del Bigio, "Biological reactions to cerebrospinal fluid shunt devices: A review of the cellular pathology," *Neurosurgery*, vol. 42, no. 2, pp. 319-325, 1998.

[6] K. Echizenya, M. Satoh, H. Murai, H. Ueno, H. Abe, and T. Komai, "Mineralization and biodegradation of CSF shunting systems," *Journal of Neurosurgery*, vol. 67, no. 4, pp. 584-591, 1987.

[7] D.J. Gower, J.C. Lewis, and D.L. Kelly, "Sterile shunt malfunction - A scanning electron-microscope perspective," *Journal of Neurosurgery*, vol. 61, no. 6, pp. 1079-1084, 1984.

[8] H. Koga, J. Mukawa, M. Nakata, O. Sakuta, and Y. Higa, "Analysis of retained ventricular shunt catheters," *Neurologia Medico-Chirurgica*, vol. 32, no. 11, pp. 824-828, 1992.

[9] J.A. Lazareff, W. Peacock, L. Holly, J. Ver Halen, A. Wong, and C. Olmstead, "Multiple shunt failures: an analysis of relevant factors," *Childs Nervous System*, vol. 14, no. 6, pp. 271-275, 1998.

[10] W.F. Schoener, C. Reparon, R. Verheggen, and E. Markakis, "Evaluation of Shunt Failures by Compliance Analysis and Inspection of Shunt Valves and Shunt Materials, Using Microscopic or Scanning Electron Microscopic Techniques," in Matsumoto S. and Tamaki N. (eds.) *Hydrocephalus: Pathogenesis and Treatment* New York: Springer-Verlag, 1991, Pp. 452-472.

[11] R.B. Snow and N. Kossovsky, "Hypersensitivity reaction associated with sterile ventriculoperitoneal shunt malfunction," *Surgical Neurology*, vol. 31, no. 3, pp. 209-214, 1989.

[12] E.C.G. Ventureyra and M.J. Higgins, "A new ventricular catheter for the prevention and treatment of proximal obstruction in cerebrospinal-fluid shunts," *Neurosurgery*, vol. 34, no. 5, pp. 924-926, 1994.

[13] N. Kossovsky and R.B. Snow, "Clinical-pathological analysis of failed centeral nervous-system fluid shunts," *Journal of Biomedical Materials Research-Applied Biomaterials*, vol. 23, no. A1, pp. 73-86, 1989.

[14] J.W. Judy and R.S. Muller, "Magnetic microactuation of torsional polysilicon structures," *Sensors and Actuators A (Physical)*, vol. A53, no. 1-4, pp. 392-396, 1996.

[15] J.W. Judy and R.S. Muller, "Magnetically Actuated, Addressable Microstructures" *IEEE Journal of Microelectromechanical Systems*, vol. 6, no. 3, pp. 249-256, 1997.

[16] D.C. Giliberti, K.A. Anderson, and K.C. Dee, "A jet impingement investigation of osteoblastic cell adhesion," *Journal of Biomedical Materials Research*, vol. 62, pp. 422-429, 2002.

[17] K.J. Bundy, L.G. Harris, B.A. Rahn, and R.G. Richards, "Measurement of fibroblast and bacterial detachment from biomaterials using jet impingement," *Cell Biology International*, vol. 25, no. 4, pp. 289-307, 2001.

[18] E.A.G. Peeters, C.W.J. Oomens, C.W.C. Bouten, D.L.Bader, and F.T.P. Baaijens, "Viscoelastic properties of single attached cells under compression," *Journal of Biomechanical Engineering*, vol. 127, pp. 237-243, 2005.